View metadata, citation and similar papers at core.ac.uk

brought to you by CORE

provided by Explore Bristol Research

Johnson, M. H., & Sahin, D. (2020). Low-loss, low-crosstalk waveguide crossing for scalable integrated silicon photonics applications. *Optics Express*. https://doi.org/10.1364/OE.381304

Publisher's PDF, also known as Version of record

License (if available):
CC BY

Link to published version (if available):
10.1364/OE.381304

Link to publication record in Explore Bristol Research
PDF-document

This is the final published version of the article (version of record). It first appeared online via OSA Publishing at https://doi.org/10.1364/OE.381304 . Please refer to any applicable terms of use of the publisher.

University of Bristol - Explore Bristol Research

General rights

This document is made available in accordance with publisher policies. Please cite only the published version using the reference above. Full terms of use are available:
http://www.bristol.ac.uk/pure/about/ebr-terms

Research Article | Vol. 28, No. 9 / 27 April 2020 / Optics Express 12498
Optics EXPRESS

Low-loss, low-crosstalk waveguide crossing for scalable integrated silicon photonics applications

MACK JOHNSON,[1,2] MARK G. THOMPSON,[1] AND DÖNDÜ SAHIN[1,*]

[1]Quantum Engineering Technology Labs, H. H. Wills Physics Laboratory, University of Bristol, Tyndall Avenue, BS8 1FD, UK
[2]Quantum Engineering Centre for Doctoral Training, H. H. Wills Physics Laboratory, University of Bristol, Tyndall Avenue, BS8 1FD, UK
*d.sahin@bristol.ac.uk

Abstract: A waveguide crossing based on multi-mode interference is designed and experimentally characterized on the silicon platform. The insertion loss of the device is measured as 43 ± 4 mdB per crossing, with a crosstalk of < -50 dB between 1550 and 1560 nm, in good agreement with predictions from 3D finite-difference time-domain simulations. Furthermore, the device backscatter was investigated using white light reflectometry and no significant backscatter was observed from 160 waveguide crossings in the time domain. In the frequency domain, the backscatter of the waveguide crossing device was measured experimentally for the first time, achieving a backscatter of -55 dB. The crossing has a footprint of 14.3 x 14.3 μm^2 and can be fabricated in a single step.

Published by The Optical Society under the terms of the Creative Commons Attribution 4.0 License. Further distribution of this work must maintain attribution to the author(s) and the published article's title, journal citation, and DOI.

1. Introduction

The silicon-on-insulator (SOI) platform is a widely used material system for integrated optics, both for quantum [1] and classical applications [2]. The high index-contrast of SOI enables light to be confined in waveguides of sub-micron dimensions, enabling high scalability. In order to achieve high density and large connectivity on-chip [3–5], in-plane waveguide crossings present one of the most important roles in an integrated photonics toolkit. An in-plane waveguide crossing is often presented as a four-port, symmetric circuit component. Waveguide crossings have seen applications in integrated quantum photonics to implement projections of 3D circuits onto 2D planar circuits for linear optical demonstrations [6,7]. In a more recent demonstration, more than 100 waveguide crossings were used in quantum information experiments with the purpose of rerouting signal and idler photons from 16 independent sources for qudit manipulation [8]. In these demonstrations, path entanglement is achieved by using a waveguide crossing to swap signal and idler photons from independent single-photon sources to bunch them together for performing quantum operations. For these applications, it is crucial that the loss of the waveguide crossings are low to maximise single-photon count rates. Furthermore, low crosstalk is desirable to avoid unwanted leakages such as signal photons leaking into idler photon channels, reducing the degree of entanglement. Other applications of the waveguide crossing in integrated photonics include neuromorphic computing with photons [5] to enable large-scale routing and photonic fan-out in conjunction with out-of-plane waveguide crossings on many layers [9] that would incur penalties with analogous electrical circuits. Most prominently, they are used in optical switches [4,10–13]. In the largest case, up to 16 x 10^3 on-chip waveguide crossings have been implemented in a 128 x 128 port optical switch [4]. In order to obtain full connectivity in an integrated circuit, the required number of waveguide crossings may scale quadratically with N

#381304 https://doi.org/10.1364/OE.381304
Journal © 2020 Received 24 Oct 2019; revised 7 Feb 2020; accepted 19 Feb 2020; published 13 Apr 2020

Optics EXPRESS

[14], where N represents the number of ports. The large numbers of these passive components can have a significant impact on the performance of devices in all of the aforementioned applications. Therefore, it is important to optimize the following performance metrics of a waveguide crossing to ensure scalability with a small footprint: the through-crossing loss (also known as the insertion loss), the crosstalk (the amount of signal that leaks into crossing waveguides) and the reflection (light which propagates in the opposite direction), which is also known as backscatter.

Various designs for waveguide crossings have been demonstrated such as direct right-angle crossings [12,15,16], multi-mode interference crossings [3,13,17–21] and sub-wavelength structures [22]. Recently, the inverse-design method [23] has been explored for optimisation of crossing structures [24–26]. Designs using this method have shown promising results, including polarisation-independent operation [26]. The drawback to the method is that the optimised resulting structures are sensitive to process variations, which limits their potential in high-throughput processing relative to conventional designs [23]. The best reported insertion loss for an SOI in-plane crossing is 7 mdB with a crosstalk level of -40 dB [20], whilst the best crosstalk is < -70 dB using a multi-mode interference crossing with rib waveguides of width 1.2 μm for injection and 2.5 μm in the multi-mode region [13]. In both cases, these structures have footprints larger than 30 x 30 μm^2. Effort has been made to improve the performance of small footprint waveguide crossings. For example, fully etched regions in the crossing center were implemented on a right-angle crossing, to act as lensing structures for refocusing at the crossing region to counteract diffraction [15]. These crossings performed with an insertion loss of < 0.3 dB and a crosstalk of -30 dB in a device with 1 x 1 μm^2 footprint. Whilst the performance of these ultra-compact crossings is still relatively high compared to the larger structures, there is potential for an in-between device with good all-round performances within a small footprint, maintaining a single fabrication step for compatibility with other fully etched structures such as strip waveguides, which are useful for integrated quantum photonic applications such as on-chip single-photon generation and detection [27–30].

In this paper, we experimentally demonstrate a multi-mode waveguide crossing on the SOI platform with a crosstalk of -50 dB and an insertion loss of 43 ± 4 mdB. The backscatter of the device was measured using white light reflectometry and no significant increase in backscatter could be found from a chain of 160 crossings as compared to a single crossing. Furthermore, the backscatter of the waveguide crossing device was extracted experimentally, achieving a level of -55 dB. The structure is fully etched into silicon in a single step, adding to its simplicity of fabrication. The structure also benefits from a small-sized footprint of 14.3 x 14.3 μm^2.

2. Design

The design is based on the SOI platform with 2 μm buried oxide and a 220 nm thick device layer. A scanning electron microscope (SEM) of the device and its footprint are shown in Fig. 1(a). The optimization of the crossing structure involves various parameters such as the multi-mode waveguide width W_M, multi-mode waveguide length L_M (blue) and the taper length L_T (grey). The input and output waveguides (green) before and after the crossing structure are all 500 nm wide. Since the crossing is based on multi-mode interference, the beat length L_B is an important length scale characterizing the interference and is given by:

$$L_B = \frac{\lambda}{2(n_0 - n_1)} \tag{1}$$

where λ is the wavelength and n_0 and n_1 are the effective indices of the fundamental and first order modes excited in the multi-mode waveguide region [31]. Figure 2(a) shows the effective indices of the fundamental and first order quasi-transverse electric (TE) and quasi-transverse magnetic (TM) modes for the range $1 \leq W_M \leq 2.2$ μm, calculated with the eigenmode solver in Lumerical FDTD solutions [32]. Using this information and Eq. (1), we calculate L_B in Fig. 2(b).

Optics EXPRESS

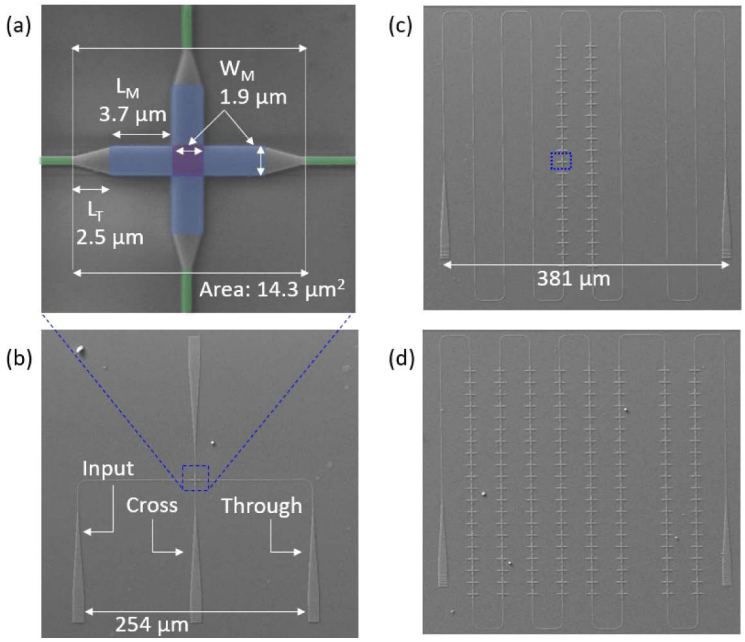

Fig. 1. SEM images of the fabricated waveguide crossing. (a) Close-up image of the multi-mode waveguide crossing with relevant dimensions. Device design for (b) crosstalk measurement and cutback measurements with (c) 40 and (d) 160 crossings, respectively, for extracting the device insertion loss. Dashed lines show an individual crosser in (c).

L_B for the TE polarization can be as small as 2 μm at W_M = 1 μm, or as large as 12 μm when W_M = 2.2 μm. For this work, we consider the TE polarization due to compatibility with the grating couplers [33], whilst data for TM polarization is included in Figs. 2(a) and 2(b) for discussions later. The reason for investigating this range of W_M was due to trying to find a structure with a footprint smaller than 15 x 15 μm^2, suitable for implementation in other works [30].

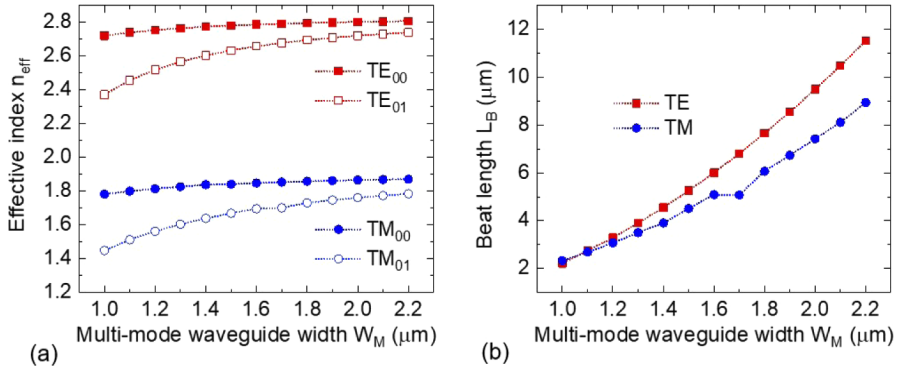

Fig. 2. (a) Calculated effective indices of the fundamental and first order TE (red) and TM (blue) modes as function of waveguide width W_M. (b) L_B as a function of W_M for TE and TM polarizations.

The field excitation in the multi-mode waveguide utilizes the symmetric interference regime [31], characterized by an input waveguide at the center of the multi-mode waveguide and selective

Optics EXPRESS

excitation of even-parity modes. The symmetric interference regime allows the device to operate with a lower L_B relative to a general multi-mode interference device, which is desirable for reducing the device footprint. The symmetric interference is shown in the electromagnetic simulation (Fig. 3(a)), whilst the associated intensity profiles for excited modes in various cross sections of the simulation window are shown in Fig. 3(b). The field evolves between TE_{00} and TE_{01} as it passes through the multi-mode waveguide, forming TE_{00} at the center of the crossing (with a peak intensity 2.1 times smaller than the input waveguide) and again at the output waveguide. The self-imaging property is utilized to reduce the device loss due to focusing at the center of the crossing, in a similar manner to other designs [3,13,17–21].

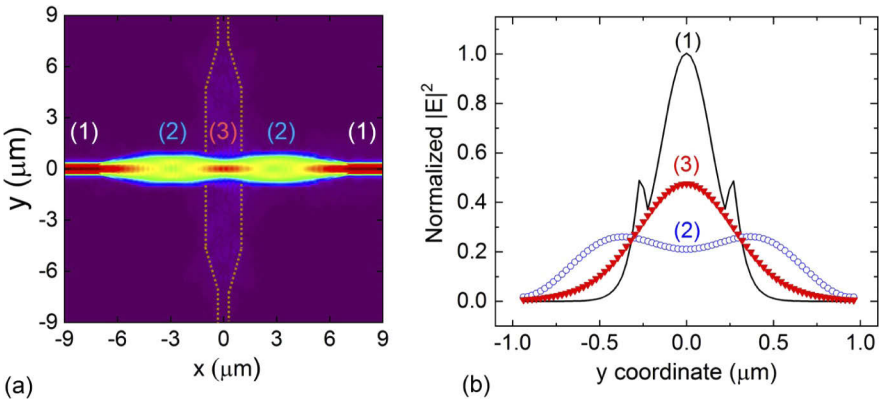

Fig. 3. (a) Electromagnetic simulation of the optimized device excited with quasi-TE mode polarization. (b) Normalized intensity profiles at points (1), (2) and (3) in (a) to show excited modes in the multi-mode waveguide. The yellow dashed lines in (a) are to guide the eye for symmetric ports of the waveguide crossing.

3D FDTD simulations were used to perform the optimization. The optimization starts with fixing L_T at 3 μm, for efficient injection efficiency into the multi-mode waveguide. Then, various iterations were made on W_M and L_M until a structure with a low insertion loss and crosstalk was found. This yielded W_M = 1.9 μm and L_M = 3.7 μm. After, L_T was swept to try and reduce the device footprint whilst maintaining good performance. This resulted with L_T = 2.5 μm. The results of the optimized device are shown in Fig. 4(a). The insertion losses of the device can be as low as 0.042 dB at λ = 1555 nm. The structure has a good performance bandwidth, showing

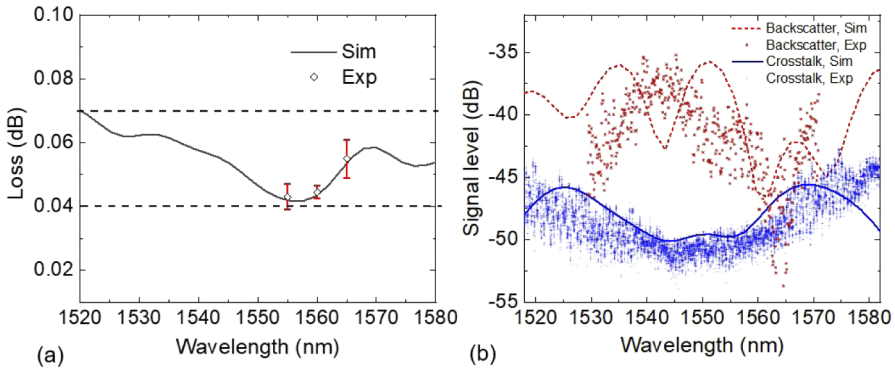

Fig. 4. Simulated (a) insertion loss, and (b) reflection and crosstalk for the optimized device. Dashed lines in (a) are to guide the eye.

Optics EXPRESS

no worse than 0.07 dB loss over the range of $1520 \leq \lambda \leq 1580$ nm. The associated crosstalk and reflection are shown in Fig. 4(b). The crosstalk is no worse than -45.6 dB in the same bandwidth as above. The highest backscatter is -35.7 dB, whilst the best case is -46.6 dB at $\lambda = 1562$ nm. According to our analysis, the associated periodicity observed in the simulated structure is due to the interference between two reflections that occur when entering and exiting the crossing region (shown in purple in Fig. 1(a)). These reflections are caused by the mismatch of the evolving TE mode in the multi-mode waveguide and the 220 nm SOI slab TE_{00} mode in the crossing region. Reducing index mismatch between these regions can be achieved by using a larger W_M and has been demonstrated with shallow etched rib waveguides of $W_M = 2.5$ μm [13]. This occurs at the expense of device footprint, due to the larger L_B as was shown in Fig. 2(b).

3. Fabrication

For experimental characterization, waveguides (shown in Figs. 1(b)–1(d)) were fabricated on SOI with 220 nm device layer thickness. The SOI surface was cleaned by oxygen plasma prior to spin-coating. For this fabrication, we used XR1541-006 resist with a spin-on thickness of 160 nm. After etching, we are left with a capping layer of 20–40 nm. XR1541-006 behaves similarly to HSQ, forming an SiO_2-like structure when developed. We used 3D FDTD to investigate the effect of the capping layer by modelling the same waveguide crossing structure on top of the Si device layer, but with SiO_2. We found no notable change in the insertion loss or crosstalk of the device with 0 to 150 nm of capping layer.

Exposure was performed with a 50 kV Raith VOYAGER electron-beam lithography system. The structures were then transferred to the silicon layer using reactive ion etching with laser endpoint interferometry. Two different sets of structures were designed to measure the crosstalk (Fig. 1(b)) and the insertion loss (Figs. 1(c) and 1(d)). In order to avoid stitching errors associated with our maximum size writefield (500 x 500 μm^2), the insertion loss measurements used a 3.8 mm waveguide connected by grating couplers with 381 μm port spacing and were patterned as cut-back measurements. The best simulated performance of Fig. 4(a) is near 0.04 dB and rises to 0.05 dB within a wavelength range of ±10 nm, meaning we expect a reduction in transmission between 1.6 and 2 dB induced by propagation through 40 waveguide crossings. For these measurements we implemented 0, 40, 80, 120 and 160 waveguide crossings. For the crosstalk measurements, three grating couplers spaced 127 μm apart were used, with the waveguide crossing centered above the second grating (see Fig. 1(b)) to extract crosstalk by inputting the laser into the input port, whilst detecting the signal in the cross and through ports.

4. Results

The insertion losses were characterized at 0 dBm laser power with a Yenista Tunics-T100S-HP tunable diode laser with an operating bandwidth of $1500 \leq \lambda \leq 1630$ nm. To ensure TE polarization was injected, a polarization controller was inserted between the laser and the fiber array. The cutback measurement has 5 different device structures ranging from 0 to 160 crosses, with a separation of 40 crossings. The results are shown in Fig. 5. This measurement was taken at a wavelength of 1560 nm due to a shift in the peak wavelength of the grating couplers. A linear fit through the data yields an insertion loss of 0.044 ± 0.002 dB per crossing, in good agreement with the simulation results predicted in Fig. 4(a). Two more fits were also performed at 1555 nm and 1565 nm. The results for these are shown in Fig. 4(a). The best performance we found was at 1555 nm, with an experimentally extracted loss of 0.043 ± 0.004 dB.

In order to extract the crosstalk, the relative signal between the through and cross ports were measured. This was achieved by finding the noise floor of the detector (Keysight N7747A) and then increasing the laser power to raise the crosstalk signal above the noise floor. Figure 6 shows the through and cross port spectrum of a device taken at 3 dBm laser power. The optimal through port coupling for this measurement was at $\lambda = 1550$ nm, showing -50.3 dB of crosstalk.

Optics EXPRESS

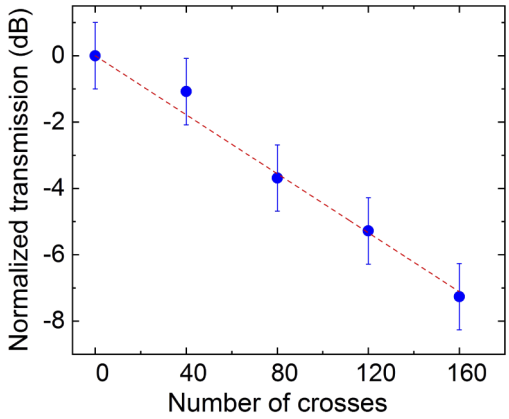

Fig. 5. Cut-back measurements for determination of the device loss. Red line is a linear fit through the data.

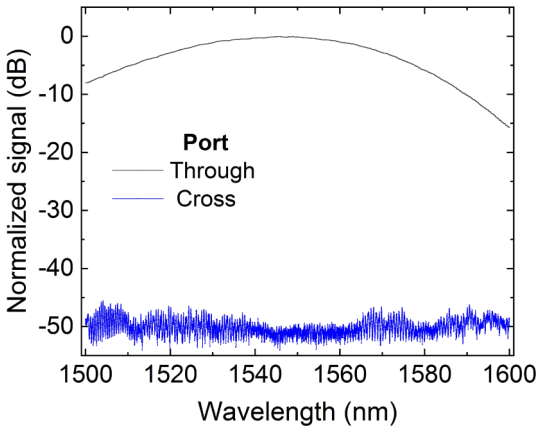

Fig. 6. Measurement of the device crosstalk.

The residual plot for the crosstalk of the same device is plotted in Fig. 4(b) for comparison with the simulation. The device operates with better than -45.8 dB crosstalk within the bandwidth of $1525 \leq \lambda \leq 1570$ nm. The best-case crosstalk is -50.3 dB at 1550 nm. The > -45.8 dB performance observed for $\lambda > 1570$ nm and $\lambda < 1525$ nm are attributed to the grating coupler performance, which can be observed from the through port transmission spectrum in Fig. 6. However, the spectrum shows good agreement with the simulation in Fig. 4(b) within the range of $1525 \leq \lambda \leq 1570$ nm.

Finally, the backscatter of the device was quantified by using a Luna OBR 4600 white light reflectometer. For experimental measurements, this replaced the laser and allows measurement between $1530 \leq \lambda \leq 1570$ nm. An example scan is shown in Fig. 7(a). To remove contributions from fiber connectors before the chip, the data is shown in a relevant 10 ns interval. A baseline signal of -125 dB can be observed until the signal reaches the chip, where a significant backscatter peak occurs at 26 ns, rising to -59.5 dB. The reflection at 28 ns is coming from the measurement set-up and was observed in all measurements irrespective of the number of crossings. The baseline can be observed to reduce to < -130 dB after the first peak at 27 ns. The backscatter peak at 26 ns was attributed to the first grating coupler. In order to verify this, a zoomed-in scan is shown in a 0.2 ns range in Fig. 7(b). The waveguide with 160 crossings and the reference zero

Optics EXPRESS

crossing waveguides were compared to discern any differences in behavior. When comparing the spectra after 26.06 ns, it can be observed that the reflected signal for the 160 crossing waveguide decays faster than the zero crossing. This is expected, since the signal has to travel through the 160 waveguide crossings twice (320 crossings in total). We also verified that this time interval corresponds to propagation in the chip through a back of the envelope calculation. The time of the flight in the chip for a pulse in the 500 nm SOI waveguide (based on a group index of 4.2 [34]) is 0.05 ns, meaning the reflected signal will be on the order of 0.1 ns, agreeing with the observation of Fig. 7(b). We also performed this measurement on the crosstalk waveguide and were able to check the spectral components of the signal within the chip from a single waveguide crossing. This is shown in Fig. 4(b). It can be observed that the device performs in the same signal level as expected from the simulation but with an offset in wavelength. We can confirm from further simulations that the offset and -55 dB performance at 1565 nm are due to small changes in structural dimensions.

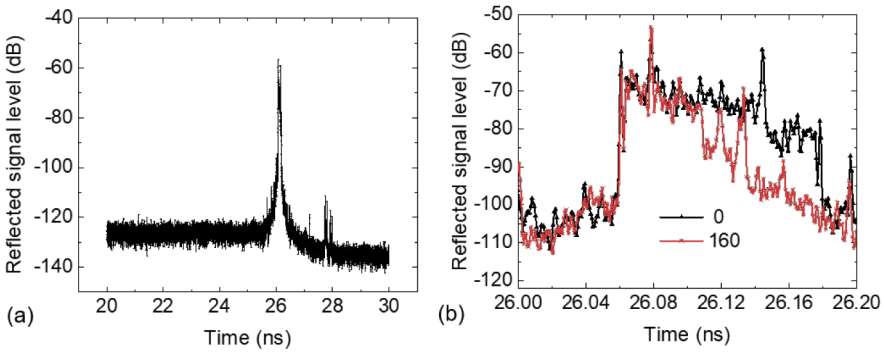

Fig. 7. Backscatter measurements. (a) Reflected signal for the device with zero crossings and (b) zoomed-in signal on the device with zero (black) and 160 (red) crossings.

To assess the fabrication tolerance of the device, the insertion loss was characterised by simulating the structure with an added bias (change in structural dimension) to one of the parameters (L_M, W_M and L_T) whilst the other two were held constant at the optimised parameters. Figure 8(a) shows the results for up to ± 50 nm of bias. The device shows good tolerance to changes in L_T and L_M within this range, showing no worse than 0.05 dB loss in the case of -50 nm of bias on L_M, whilst losses below 0.043 dB were observed for up to ± 100 nm of bias on L_T. W_M induces the largest changes in insertion loss, increasing to > 0.06 dB for biases greater than ± 30 nm. This change is attributed to W_M giving rise to changes in L_B (as shown in Fig. 2(b)), which shift the optimal transmission wavelength of the device. Figure 8(b) shows the wavelength shift as a function of fabrication bias for all three parameters. W_M biases induce the largest shift, with up to 50 nm of wavelength shift for ± 50 nm of fabrication bias.

Finally, Table 1 compares the results of this work with other experimental results for waveguide crossing structures. While strip waveguide designs as presented in this work are compatible with single step fabrication processes, rib waveguides as in Ref. [13] require an extra fabrication step. For simplicity, this is avoided in this work. Although the work of Refs. [20] and [13] present an improvement on insertion losses and crosstalk respectively, these designs increase the footprint by over a factor of 4. When compared to the smaller designs, the insertion loss is only improved on by Ref. [19], with a trade-off in crosstalk. In terms of backscatter, the present work is the only work in Table 1 to experimentally measure backscattering from a waveguide crossing device.

Optics EXPRESS

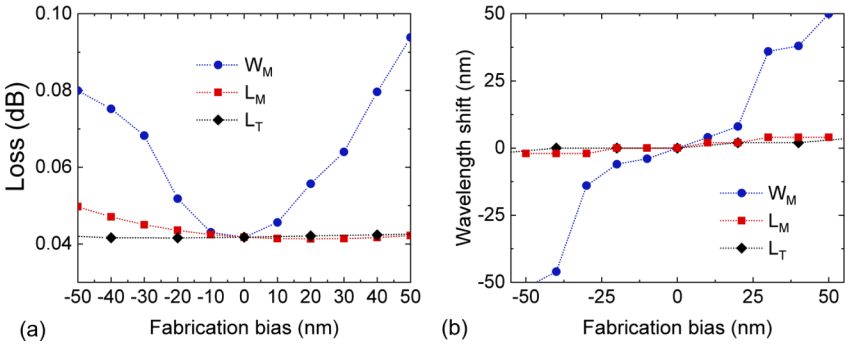

Fig. 8. (a) Insertion loss as a function of fabrication bias for the three waveguide crossing parameters and (b) best-case transmission wavelength shift as a function of fabrication bias.

Table 1. Comparisons of experimental results for SOI waveguide crossings. N/A: not measured, SWG: sub-wavelength waveguide. * means dimension information not given.

Reference	Footprint (μm^2)	Insertion loss (dB)	Crosstalk (dB)	Backscatter (dB)	Waveguide Type
Dumais [20]	30 x 30	0.007	−40	N/A	500 nm strip
Ma [19]	9 x 9	0.028	−37	N/A	500 nm strip
Celo [21]	6.5 x 6.5	0.11	−45	N/A	strip*
Seok [13]	31 x 31	0.017	−55	N/A	1.2 μm rib
Han [15]	1 x 1	0.28	−30	N/A	500 nm strip
Bock [22]	< 1 x 1	0.023	−40	N/A	400 nm SWG
Yu [26]	3 x 3	0.20	−28	N/A	strip*
This work	14.3 x 14.3	0.043	−50	−55	500 nm strip

5. Discussion

We have experimentally demonstrated a small footprint waveguide crossing on SOI with 43 ± 4 mdB insertion loss, -55 dB backscatter and -50 dB crosstalk in the telecom band. The small device footprint, less than 15 x 15 μm^2, is critical for us as it will be implemented into a cavity enhanced superconducting nanowire single-photon detector design originally presented in [30] without inducing significant performance degradation. However, the device presented here will be useful in various applications such as optical switching [4,10–13], neuromorphic computing [5] and quantum computing [6–8], that will be scaled up to large numbers of components in the future. The accumulation of many components sets stringent requirements for the performance of a device on the single-component level. Also, since many crossings need to be fabricated, the simplicity of the fabrication process as proposed here becomes important for maintaining reasonable tolerances. Improvements may also be made to the design here by implementing fully etched index-matching regions in the center of the waveguide crossing. Such an idea has been implemented with great results using right-angled waveguide crossings [15] to decrease the insertion loss. On the other hand, a polarization-independent crossing could be realised through using sub-wavelength structures to engineer the TE and TM modes in Fig. 2(a) for beat length matching, as was demonstrated for a directional coupler [35].

6. Conclusion

A multi-mode waveguide crossing on the SOI platform was designed and experimentally tested. The crossing has an experimentally determined insertion loss of 43 mdB and crosstalk of less than -50 dB as suggested by FDTD simulations. The backscatter of the device was experimentally

Optics EXPRESS

characterised for the first time and was shown to be no worse than -35 dB, with a best case of -55 dB in the frequency domain. In the time domain, no significant distinguishable signals were observed when measuring the backscatter of 160 crossings on a waveguide.

Funding

Engineering and Physical Sciences Research Council (EP/K03308S/1, EP/L015730/1, EP/L024020/1, EP/M013472/1, EP/N015126/1).

Acknowledgments

The authors thank Pisu Jiang for assistance and discussion in the fabrication process, Stefano Paesani and Raffaele Santagati for useful discussions relating to the applications of the waveguide crossing for integrated quantum photonics.

Disclosures

The authors declare no conflicts of interest.

References

1. J. W. Silverstone, D. Bonneau, J. L. O'Brien, and M. G. Thompson, "Silicon quantum photonics," IEEE J. Sel. Top. Quantum Electron. **22**(6), 390–402 (2016).
2. X. Tu, C. Song, T. Huang, Z. Chen, and H. Fu, "State of the art and perspectives on silicon photonic switches," Micromachines **10**(1), 51 (2019).
3. S. Han, T. J. Seok, N. Quack, B.-W. Yoo, and M. C. Wu, "Large-scale silicon photonic switches with movable directional couplers," Optica **2**(4), 370–375 (2015).
4. K. Kwon, T. J. Seok, J. Henriksson, J. Luo, L. Ochikubo, J. Jacobs, R. S. Muller, and M. C. Wu, "128× 128 silicon photonic mems switch with scalable row/column addressing," in *CLEO: Science and Innovations*, (Optical Society of America, 2018), pp. SF1A–4.
5. J. M. Shainline, S. M. Buckley, R. P. Mirin, and S. W. Nam, "Superconducting optoelectronic circuits for neuromorphic computing," Phys. Rev. Appl. **7**(3), 034013 (2017).
6. J. Wang, D. Bonneau, M. Villa, J. W. Silverstone, R. Santagati, S. Miki, T. Yamashita, M. Fujiwara, M. Sasaki, H. Terai, M. G. Tanner, C. M. Natarjan, R. H. Hadfield, J. L. O'Brien, and M. G. Thompson, "Chip-to-chip quantum photonic interconnect by path-polarization interconversion," Optica **3**(4), 407–413 (2016).
7. R. Santagati, J. W. Silverstone, M. Strain, M. Sorel, S. Miki, T. Yamashita, M. Fujiwara, M. Sasaki, H. Terai, M. G. Tanner, C. M. Natarjan, R. H. Hadfield, J. L. O'Brien, and M. G. Thompson, "Silicon photonic processor of two-qubit entangling quantum logic," J. Opt. **19**(11), 114006 (2017).
8. J. Wang, S. Paesani, Y. Ding, R. Santagati, P. Skrzypczyk, A. Salavrakos, J. Tura, R. Augusiak, L. Mančinska, D. Bacco, D. Bonneau, J. W. Silverstone, Q. Gong, A. Acin, K. Rottwitt, L. K. Oxenlowe, J. L. O'Brien, A. Laing, and M. G. Thompson, "Multidimensional quantum entanglement with large-scale integrated optics," Science **360**(6386), 285–291 (2018).
9. J. Chiles, S. Buckley, N. Nader, S. W. Nam, R. P. Mirin, and J. M. Shainline, "Multi-planar amorphous silicon photonics with compact interplanar couplers, cross talk mitigation, and low crossing loss," APL Photonics **2**(11), 116101 (2017).
10. L. Lu, S. Zhao, L. Zhou, D. Li, Z. Li, M. Wang, X. Li, and J. Chen, "16× 16 non-blocking silicon optical switch based on electro-optic mach-zehnder interferometers," Opt. Express **24**(9), 9295–9307 (2016).
11. L. Qiao, W. Tang, and T. Chu, "32× 32 silicon electro-optic switch with built-in monitors and balanced-status units," Sci. Rep. **7**(1), 42306 (2017).
12. L. Chen and Y.-K. Chen, "Compact, low-loss and low-power 8× 8 broadband silicon optical switch," Opt. Express **20**(17), 18977–18985 (2012).
13. T. J. Seok, N. Quack, S. Han, R. S. Muller, and M. C. Wu, "Large-scale broadband digital silicon photonic switches with vertical adiabatic couplers," Optica **3**(1), 64–70 (2016).
14. D. Nikolova, D. M. Calhoun, Y. Liu, S. Rumley, A. Novack, T. Baehr-Jones, M. Hochberg, and K. Bergman, "Modular architecture for fully non-blocking silicon photonic switch fabric," Microsyst. Nanoeng. **3**(1), 16071 (2017).
15. H.-L. Han, H. Li, X.-P. Zhang, A. Liu, T.-Y. Lin, Z. Chen, H.-B. Lv, M.-H. Lu, X.-P. Liu, and Y.-F. Chen, "High performance ultra-compact soi waveguide crossing," Opt. Express **26**(20), 25602–25610 (2018).
16. W. Bogaerts, P. Dumon, D. Van Thourhout, and R. Baets, "Low-loss, low-cross-talk crossings for silicon-on-insulator nanophotonic waveguides," Opt. Lett. **32**(19), 2801–2803 (2007).
17. H. Chen and A. W. Poon, "Low-loss multimode-interference-based crossings for silicon wire waveguides," IEEE Photonics Technol. Lett. **18**(21), 2260–2262 (2006).

Optics EXPRESS

18. Y. Zhang, A. Hosseini, X. Xu, D. Kwong, and R. T. Chen, "Ultralow-loss silicon waveguide crossing using bloch modes in index-engineered cascaded multimode-interference couplers," Opt. Lett. **38**(18), 3608–3611 (2013).
19. Y. Ma, Y. Zhang, S. Yang, A. Novack, R. Ding, A. E.-J. Lim, G.-Q. Lo, T. Baehr-Jones, and M. Hochberg, "Ultralow loss single layer submicron silicon waveguide crossing for soi optical interconnect," Opt. Express **21**(24), 29374–29382 (2013).
20. P. Dumais, D. Goodwill, D. Celo, J. Jiang, and E. Bernier, "Three-mode synthesis of slab gaussian beam in ultra-low-loss in-plane nanophotonic silicon waveguide crossing," in *2017 IEEE 14th International Conference on Group IV Photonics (GFP)*, (IEEE, 2017), pp. 97–98.
21. D. Celo, D. Goodwill, P. Dumais, J. Jiang, and E. Bernier, "Low-loss waveguide crossings for photonic integrated circuits on soi technology," in *11th International Conference on Group IV Photonics (GFP)*, (IEEE, 2014), pp. 189–190.
22. P. J. Bock, P. Cheben, J. H. Schmid, J. Lapointe, A. Delâge, D.-X. Xu, S. Janz, A. Densmore, and T. J. Hall, "Subwavelength grating crossings for silicon wire waveguides," Opt. Express **18**(15), 16146–16155 (2010).
23. S. Molesky, Z. Lin, A. Y. Piggott, W. Jin, J. Vucković, and A. W. Rodriguez, "Inverse design in nanophotonics," Nat. Photonics **12**(11), 659–670 (2018).
24. L. Lu, M. Zhang, F. Zhou, W. Chang, J. Tang, D. Li, X. Ren, Z. Pan, M. Cheng, and D. Liu, "Inverse-designed ultra-compact star-crossings based on phc-like subwavelength structures for optical intercross connect," Opt. Express **25**(15), 18355–18364 (2017).
25. G. B. Hoffman, C. Dallo, A. Starbuck, D. Hood, A. Pomerene, D. Trotter, and C. T. DeRose, "Improved broadband performance of an adjoint shape optimized waveguide crossing using a levenberg-marquardt update," Opt. Express **27**(17), 24765–24780 (2019).
26. Z. Yu, A. Feng, X. Xi, and X. Sun, "Inverse-designed low-loss and wideband polarization-insensitive silicon waveguide crossing," Opt. Lett. **44**(1), 77–80 (2019).
27. J. E. Sharping, K. F. Lee, M. A. Foster, A. C. Turner, B. S. Schmidt, M. Lipson, A. L. Gaeta, and P. Kumar, "Generation of correlated photons in nanoscale silicon waveguides," Opt. Express **14**(25), 12388–12393 (2006).
28. N. C. Harris, D. Bunandar, M. Pant, G. R. Steinbrecher, J. Mower, M. Prabhu, T. Baehr-Jones, M. Hochberg, and D. Englund, "Large-scale quantum photonic circuits in silicon," Nanophotonics **5**(3), 456–468 (2016).
29. D. Grassani, S. Azzini, M. Liscidini, M. Galli, M. J. Strain, M. Sorel, J. Sipe, and D. Bajoni, "Micrometer-scale integrated silicon source of time-energy entangled photons," Optica **2**(2), 88–94 (2015).
30. N. A. Tyler, J. Barreto, G. E. Villarreal-Garcia, D. Bonneau, D. Sahin, J. L. O'Brien, and M. G. Thompson, "Modelling superconducting nanowire single photon detectors in a waveguide cavity," Opt. Express **24**(8), 8797–8808 (2016).
31. L. B. Soldano and E. C. Pennings, "Optical multi-mode interference devices based on self-imaging: principles and applications," J. Lightwave Technol. **13**(4), 615–627 (1995).
32. "Lumerical inc. http://www.lumerical.com/products/," (Last accessed : August 2019).
33. Y. Ding, H. Ou, and C. Peucheret, "Ultrahigh-efficiency apodized grating coupler using fully etched photonic crystals," Opt. Lett. **38**(15), 2732–2734 (2013).
34. E. Dulkeith, F. Xia, L. Schares, W. M. Green, and Y. A. Vlasov, "Group index and group velocity dispersion in silicon-on-insulator photonic wires," Opt. Express **14**(9), 3853–3863 (2006).
35. L. Liu, Q. Deng, and Z. Zhou, "Subwavelength-grating-assisted broadband polarization-independent directional coupler," Opt. Lett. **41**(7), 1648–1651 (2016).

51.6.155.63 {ts '2020-04-20 09:42:18'}